Towards a multi-fidelity & multi-objective Bayesian optimization efficient algorithm

Rémy Charayron, Thierry Lefebvre, Nathalie Bartoli, Joseph Morlier

To cite this version:

Rémy Charayron, Thierry Lefebvre, Nathalie Bartoli, Joseph Morlier. Towards a multi-fidelity & multi-objective Bayesian optimization efficient algorithm. Aerospace Science and Technology, 2023, 142 (Part B), 10.1016/j.ast.2023.108673 . hal-04254361

HAL Id: hal-04254361
https://hal.science/hal-04254361

Submitted on 23 Oct 2023

Towards a multi-fidelity & multi-objective Bayesian optimization efficient algorithm

Rémy Charayron[a,b], Thierry Lefebvre[a], Nathalie Bartoli[a], Joseph Morlier[b]

[a] *ONERA/DTIS, Université de Toulouse, 2 avenue Edouard Belin, Toulouse, 31400, France*

[b] *ICA, Université de Toulouse, ISAE-SUPAERO, MINES ALBI, UPS, INSA, CNRS, 3 rue Caroline Aigle, Toulouse, 31400, France*

Abstract

Black-box optimization methods like Bayesian optimization are often employed in cases where the underlying objective functions and their gradient are complex, expensive to evaluate, or unavailable in closed form, making it difficult or impossible to use traditional optimization techniques. Fixed-wing drone design problems often face this kind of situations. Moreover in the literature multi-fidelity strategies allow to consistently reduce the optimization cost for mono-objective problems. The purpose of this paper is to propose a multi-fidelity Bayesian optimization method that suits to multi-objective problem solving. In this approach, low-fidelity and high-fidelity objective functions are used to build co-Kriging surrogate models which are then optimized using a Bayesian framework. By combining multiple fidelity levels and objectives, this approach efficiently explores the solution space and identifies the set of Pareto-optimal solutions. First, four analytical problems were solved to assess the methodology. The approach was then used to solve a more realistic problem involving the design of a fixed-wing drone for a specific mission. Compared to the mono-fidelity strategy, the multi-fidelity one significantly improved optimization performance. On the drone test case, using a fixed budget, it allows to divide the inverted generational distance metric by 6.87 on average.

Keywords: Bayesian optimization, Multi-fidelity, Multi-objective, Multi-disciplinary optimization, Kriging, Fixed-wing drone

---

1. Introduction

Fixed-wing drones, are a significant advancement in the field of drone technology. Unlike their rotary-wing counterparts, they have a wing structure similar to traditional airplanes, enabling them to achieve sustained and efficient flight. They are characterized by their improved stability, longer flight endurance, and increased payload capacity. Then, fixed-wing drones have revolutionized the way we approach tasks that require extensive coverage and endurance in the aerial domain. Thanks to their characteristics, fixed-wing aircraft drones have become increasingly popular in recent years and have found versatile applications in various industries such as military [1, 2] for target tracking, agriculture [3, 4] for crop imaging, earth observation [5] (bathymetry, geodesy, ...), biodiversity monitoring [6] (species sampling) or infrastructure monitoring [7, 8] of high-voltage lines. As the demand for drone technology continues to grow, there is a need to ensure that the design, performance, and operation of these vehicles are optimized for their intended applications. Multi-disciplinary design optimization (MDO) [9] is a technique that combines multiple engineering disciplines to improve the overall performance of a system by solving the complex coupling between the disciplines. Elucidating the coupling between the disciplines is called solving a multi-disciplinary design analysis (MDA). A multi-disciplinary approach is necessary to ensure that the disciplines are considered and optimized in a coordinated manner. In the context of drone technology, leveraging MDO allows to create fixed-wing drones that are optimized for their purposeful applications, providing improved performance, efficiency, and safety by considering disciplines such as aerodynamic, structure, propulsion, intended mission, operational safety,...

In fixed-wing drone design like in many real-world applications, there are multiple objectives that need to be considered simultaneously, and these objectives may be conflicting. For example, increasing the manufacturing cost of a drone may be necessary to achieve greater efficiency; or the increase of drone's performance for some applications may reduce the performance for other applications. In this work we will consider constrained multi-objective problems such as:

$$\min_{x\in\Omega\subset\mathbb{R}^d} \quad \mathbf{f}(x) := [f_1(x), ...f_{n_{obj}}(x)]^T \tag{1}$$
$$\text{such that} \begin{cases} \mathbf{g_i}(x) \leq 0 \\ \mathbf{g_e}(x) = 0 \end{cases}$$

where d is the number of dimensions, $\mathbf{f}$ gathers the n_{obj} multiple objective functions f_1 to $f_{n_{obj}}$, $\mathbf{g_e}$ represents equality constraints and $\mathbf{g_i}$ inequality constraints. These problems are difficult to solve, especially when the functions are expensive-to-evaluate black-boxes (complex models, wind tunnel experiments) and have many local optima which can be the case in the drone design context. Bayesian optimization [10] is a powerful approach in this context. In [11] the authors used a Bayesian optimization framework to solve multidisciplinary, single-fidelity and single-objective optimization problems for aircraft design. Next, Bayesian optimization approach also showed good results solving multi-objective problems [12, 13]. It is likely that using a multi-fidelity Bayesian optimization approach regarding multi-objective problems will further reduce the computational cost of the overall optimization, as is the case for single-objective problems [14, 15, 16, 17, 18, 19]. Some works started to investigate the interest of using multi-fidelity Bayesian optimization to solve multi-objective problems [20, 21, 22, 23, 24, 25, 26, 27]. In [22] the fidelity level is considered as a continuous variable of the problem and is applied only on unconstrained problems. The method from [27] is also applied on unconstrained problems. In [26], the authors proposed two multi-fidelity and multi-objective criteria, one aggregating the variable fidelity expected improvement matrix through a simplified hypervolume based aggregation scheme and the other using a modified hypervolume definition. The objective of this study is to build upon these approaches and to apply the proposed method to a constrained multi-disciplinary fixed-wing drone design optimization problem. First, Section 2 recalls multi-fidelity Kriging and a mono-objective multi-fidelity Bayesian optimization method called MFSEGO (Multi-Fidelity Super Efficient Global Optimization). Next, in Section 3 we start by describing a multi-objective, mono-fidelity Bayesian optimization method named MO-SEGO (Multi-Objective Super Efficient Global Optimization). Then we propose an extension of this method to multi-fidelity & multi-objective Bayesian optimization method (MFMO-SEGO). Afterwards, Section 4 defines the analytical test cases, their experimental setup and associated results. Parallely, Section 5 proposes a test case for a fixed-wing drone in the specific category, with associated experimental setup and results. The specific category covers moderate-risk operations. Finally, Section 6 concludes and discusses these results.

2. A review of existing multi-fidelity Kriging for efficient global optimization

In this section we present multi-fidelity Kriging and the Multi-Fidelity Super Efficient Global Optimization (MFSEGO) method. This algorithm is an elementary building block for the methodology proposed in the following. The method is presented in such a way that the reader is assumed to be familiar with the Gaussian process (GP) interpolation technique, also known as Kriging models [28, 29, 30], as well as with classical Bayesian single-fidelity optimization methods based on Kriging, such as the Efficient Global Optimization (EGO) algorithm [31] for unconstrained problems and the Super Efficient Global Optimization (SEGO) algorithm [32, 33, 34] for constrained problems.

2.1. Multi-Fidelity Kriging

The Kriging model was extended to handle multivariate functions through the co-Kriging technique, which was first developed in geostatistics by [35, 36]. Later, [37] proposed a method of simplifying multi-fidelity problems by assuming relationships between different levels of accuracy. In this section, we focus on Le Gratiet's recursive formulation [38, 39], which we used to construct multi-fidelity Kriging models. This strategy ensures better prediction capabilities than its predecessors by considering the low-fidelity functions in the Kriging regression term. Suppose we have $L+1$ levels of fidelity to approach the f function, labeled f_0 through f_L from lowest to highest, and $L+1$ corresponding design of experiments (DoE), one for each fidelity level denoted $(D_i)_{i=0\ldots L}$ with $D_i = ((x_0, f_i(x_0)), ..., (x_j, f_i(x_j)), ..., (x_{N_i}, f_i(x_{N_i})))^T$, N_i being the number of points in D_i. The same philosophy can also be applied to the constraint functions $\mathbf{g_i}$ and $\mathbf{g_e}$. We assume that the DoEs are nested, meaning that every point evaluated at a higher fidelity level is also evaluated at all the lower fidelity levels: $D_L^x \subseteq D_{L-1}^x \subseteq \ldots \subseteq D_0^x$ where $D_i^x = (x_0, ..., x_j, ..., x_{N_i})^T$ corresponds to the inputs part of D_i. This nesting property helps to express the surrogate model variance in a closed form. To link the different fidelity levels, we use an assumption first introduced by [37] for the bi-fidelity case.

$$f_{l+1}(x) = \rho_l f_l(x) + \delta_{l+1}(x) \quad \text{such that} \quad f_l \perp \delta_{l+1} \quad \forall l = 0, ..., L-1 \tag{2}$$

where $\delta_{l+1}(x)$ is a discrepancy function that captures the difference between the $l+1$-th and the l-th fidelity levels while ρ_l is a scaling factor applied to f_l.
Le Gratiet [38, 39] suggested including the lower fidelity function in the set of basis functions $(h_i)_{i=1...p}$ used in the universal Kriging regression term. Then each fidelity level regression term (i.e: mean *a priori*) is written as follows:

$$\mu_{l+1}(x) = \sum_{i=1,...,p} \Big(\beta_i h_i(x) \Big) + \beta_{\rho_l} f_l(x) \quad \forall l = 0, ..., L-1 \tag{3}$$

The parameters β_{ρ_l} serve as estimates for ρ_l, while $(\beta_i)_{i=1...p}$ represents a group of unspecified multiplier coefficients. To determine these coefficients, likelihood maximization [40, 41] is employed. Assuming that a nested DoE structure was implemented, the surrogate model's fidelity levels are deemed independent. This allows to derive a recursive formulation [38, 39] for the mean ($\hat{\mu}_{l+1}$) and variance ($\hat{\sigma}^2_{l+1}$) of each GP surrogate model at a given fidelity level:

$$\forall l = 0, ..., L-1 \qquad \begin{cases} \hat{\mu}_{l+1} = \rho_l \hat{\mu}_l + \hat{\mu}_{\delta_{l+1}} \\ \hat{\sigma}^2_{l+1} = \rho_l^2 \hat{\sigma}^2_l + \hat{\sigma}^2_{\delta_{l+1}} \end{cases} \tag{4}$$

In this case, we treat ρ_l as a constant even though it may vary based on x, i.e., $\rho_l : x \mapsto \rho_l(x)$ [19]. The learning process consists in training each fidelity level separately which allows for parallelization. Since the variances can be expressed using a closed form expression, the contribution of each fidelity level to the overall variance of the multi-fidelity surrogate model can be found. This is one of the Le Gratiet's recursive formulation most significant benefit. Denoting $\sigma^2_{cont}(l, x)$ as the variance contribution of the l^{th} fidelity level at point x, and $\sigma^2_{\delta_0}$ as σ^2_0, we have:

$$\forall l = 0, ..., L-1 \quad \sigma^2_{cont}(l, x) = \sigma^2_{\delta_l}(x) \prod_{j=l}^{L-1} \rho_j^2 \quad \text{and} \quad \sigma^2_{cont}(L, x) = \sigma^2_{\delta_L}(x) \tag{5}$$

This expression of the variance contribution will be useful to the fidelity level choice at each iteration of the Bayesian optimization process. This multi-fidelity Kriging (MFK) model is available in the Surrogate Modelling

Toolbox (SMT) [42]. SMT also provides an extension of MFK that makes use of the Partial Least Square dimension reduction technique (MFKPLS) in order to tackle high dimension. MFKPLS adapts the Kriging with partial least square (KPLS) technique [43] relying on the PLS method [44, 45] to multi-fidelity. The PLS analysis performs a base change allowing to pass from input variables to latent variables. Only the first latent variables, which are those that explain the most variance, are kept. Then every point expressed in the initial space can be projected on the truncated latent space reducing the number of dimensions. Using too much latent variables does not improve the precision since almost all of the variance is captured by a lower number of latent variables. On the other hand, not using enough of them will strongly reduce the prediction capability of the model. The only difference between KPLS and MFKPLS is that for MFKPLS, the PLS analysis step to find the latent space is not applied on all of the dataset but only on the HF dataset in order to ensure robustness to poor correlations between the fidelity levels. Next the projection step is the same as in KPLS and it applies on HF and LF datasets. Now that we described the multi-fidelity Kriging model that is used in this work, lets explain the mono-objective & multi-fidelity super efficient global optimization methodology.

2.2. Multi-Fidelity Super Efficient Global Optimization

To perform multi-fidelity Bayesian optimization, one needs to determine the most promising point and the appropriate fidelity level at which to evaluate it. The approach in works such as [19, 14, 15, 16] involves breaking this problem down into two steps. First, a classical acquisition function is optimized to find the point, as in mono-fidelity Bayesian optimization:

$$x^* = \arg\max_{x\in\Omega} \alpha(x) \quad \text{with} \quad x \in \Omega_{\mathbf{g_e}} \cap \Omega_{\mathbf{g_i}} \tag{6}$$

where α is a mono-fidelity acquisition function (also called infill criterion). The most common acquisition functions are the expected improvement (EI) or the probability of improvement (PI). It also exists some regularized infill criteria like Watson and Barnes 2 ($WB2$) [46] and scaled Watson and Barnes 2 ($WB2S$) [47]. Constraint management is handled in the same way [33, 34, 47, 32] by building co-Kriging models for the constraints and searching at each iteration the new point to add optimizing the acquisition function on a feasible domain $\Omega_{\mathbf{g_i}} \cap \Omega_{\mathbf{g_e}}$ where $\Omega_{\mathbf{g_i}} = \{x, \alpha_{\mathbf{g_i}}(x) = 0\}$ and $\Omega_{\mathbf{g_e}} = \{x, \alpha_{\mathbf{g_e}}(x) \leq 0\}$. The feasibility criteria $\alpha_{\mathbf{g_e}} : \mathbb{R}^d \to \mathbb{R}^p$ and $\alpha_{\mathbf{g_i}} : \mathbb{R}^d \to \mathbb{R}^m$ (p

equality and m inequality constraints) are usually defined with the posterior means of the GPs that modelize the constraints as feasibility criterion: $\alpha_{\mathbf{g_e}} = \hat{\mu}_{\mathbf{g_e}}$ and $\alpha_{\mathbf{g_i}} = \hat{\mu}_{\mathbf{g_i}}$.

Then, the variance contribution to each fidelity level is analyzed to make an informed decision on which fidelity level to use. To be more specific, let $c_0, ..., c_L$ represent the querying costs associated with all fidelity levels $f_0, ..., f_L$, respectively. Additionally, let $\sigma^2_{red}(l, x^*)$ denote the variance reduction of the high fidelity model when the point x^* is evaluated using all fidelity levels $\leq l$, in order to maintain the nested DoE structure

$$\sigma^2_{red}(l, x^*) = \sum_{i=0}^{l} \sigma^2_{\delta_i}(x^*) \prod_{j=i}^{L-1} \rho_j^2 \tag{7}$$

In [38] the author first introduced a strategy to select the fidelity level of enrichment by penalizing the uncertainty reduction by the computational cost. Next, [19] proposed to penalize the variance reduction (which is the standard deviation squared) by the cost squared which leads to the following enrichment level criterion used in [14, 15, 16].

$$l^* = \underset{l \in 0,\dots,L}{\arg\max} \; \frac{\sigma^2_{red}(l, x^*)}{(\sum_{i=0}^{l} c_i)^2} \tag{8}$$

Eq.(8) represents a compromise between reducing variance and minimizing computational cost. The cost ratios between the various fidelity levels are therefore crucial parameters in this approach. This two-step process [14, 19] is referred to as Multi-Fidelity Super Efficient Global Optimization (MF-SEGO). In the next section multi-objective handling will be addressed.

3. New theoretical developments for Multi-Fidelity & Multi-Objective Super Efficient Global Optimization

In this section, we start by recalling and explaining the mono-fidelity, multi-objective super efficient global optimization, then we extend this methodology to the multi-fidelity case.

3.1. Mono-Fidelity, Multi-Objective Super Efficient Global Optimization

Compared to mono-fidelity & mono-objective Bayesian optimization, there are two main changes when using mono-fidelity & multi-objective Bayesian optimization. First, surrogate models must be constructed for each of the objectives. Second, the chosen infill criteria must be adapted to the multi-objective case. Several multi-objective infill criteria exist in the literature, most of the time they are extensions of mono objective infill criteria. For example, the probability of improvement (PI) [48] is extended to the minimal probability of improvement (MPI) [49], the expected hypervolume improvement ($EHVI$) [50, 51] derives from the expected improvement (EI) [31], the Pareto active learning (PAL) criterion [52, 53] from the upper confidence bound (UCB) criterion, and the multi-objective stepwise uncertainty reduction criterion [54] from the stepwise uncertainty reduction criterion (SUR) [55]. Let $\alpha_{\mathbf{f}}$ be one of these multi-objective infill criteria, in [12] the authors extend the $WB2S$ regularized infill criterion [47] to multi-objective by using the $\alpha_{\mathbf{f}}$ multi-objective infill criterion in the $WB2S$ formula:

$$\alpha_{WB2S,\alpha_{\mathbf{f}}} = \lambda\alpha_{\mathbf{f}} - \psi(\hat{\mu}_{\mathbf{f}}(x)) \tag{9}$$

$\lambda \in \mathbb{R}$ is a constant parameter and $\hat{\mu}_{\mathbf{f}} : \mathbb{R}^d \longrightarrow \mathbb{R}^{n_{obj}}$ is the GP prediction of all of the objectives gathered in $\mathbf{f}$. $\psi : \mathbb{R}^{n_{obj}} \longrightarrow \mathbb{R}$ is a scalarization operator on the different objective predictions. For example, ψ could be a maximization function or a sum function.

In this paper, we used the $WB2S$ regularized multi-objective criterion from [12]. We could couple it with various subcriteria such as PI, MPI or $EHVI$. In this work we decided to use MPI ($MPI = \alpha_{\mathbf{f}}$) as it gives the best results. Hence we describe the MPI infill criterion in the following. To do so we need to introduce some definitions. Let PS be the current approximation of the Pareto set. $x_1 \prec x_2$ means that x_1 dominates x_2. $x_1 \parallel x_2$ means that x_1 and x_2 are mutually non-dominated. $x_1 \preceq x_2$ translates into x_1 is non-dominated by x_2. It can either mean that x_1 dominates x_2 or that x_1 and x_2 are mutually non-dominated by each other. As a recall, the minimal probability of improvement at a point x ($MPI(x)$) is defined as the minimal probability (over all of the points of the Pareto set) that the point x is non dominated by the current point of the Pareto set:

$$MPI(x) = \min_{u \in PS} \mathbb{P}(x \preceq u) \tag{10}$$

This MPI criterion can be expressed in closed form as follow:

$$MPI(x) = \min_{u \in PS} \mathbb{P}(x \preceq u) = \min_{u \in PS} \left(1 - \prod_{i=1 \ldots n_{obj}} \Phi\left(\frac{\hat{y}_i(x) - y_i(u)}{\hat{\sigma}_i(x)}\right)\right) \tag{11}$$

Now that we recalled the mono-fidelity multi-objective methodology, we can extend it to multi-fidelity.

3.2. Extension to Multi-Fidelity & Multi-Objective Super Efficient Global Optimization

Our methodology called MFMO-SEGO for Multi-Fidelity & Multi-Objective Super Efficient Global Optimization relies on both the MFSEGO methodology [16, 15, 14, 19] described in Section 2.2 and the single fidelity multi-objective SEGO methodology [12] described in Section 3.1. We mixed these two methods in order to be able to tackle constrained multi-fidelity & multi-objective, black-box optimization problems. The proposed algorithm MFMO-SEGO is summarized with the help of a diagram in Fig. 1.

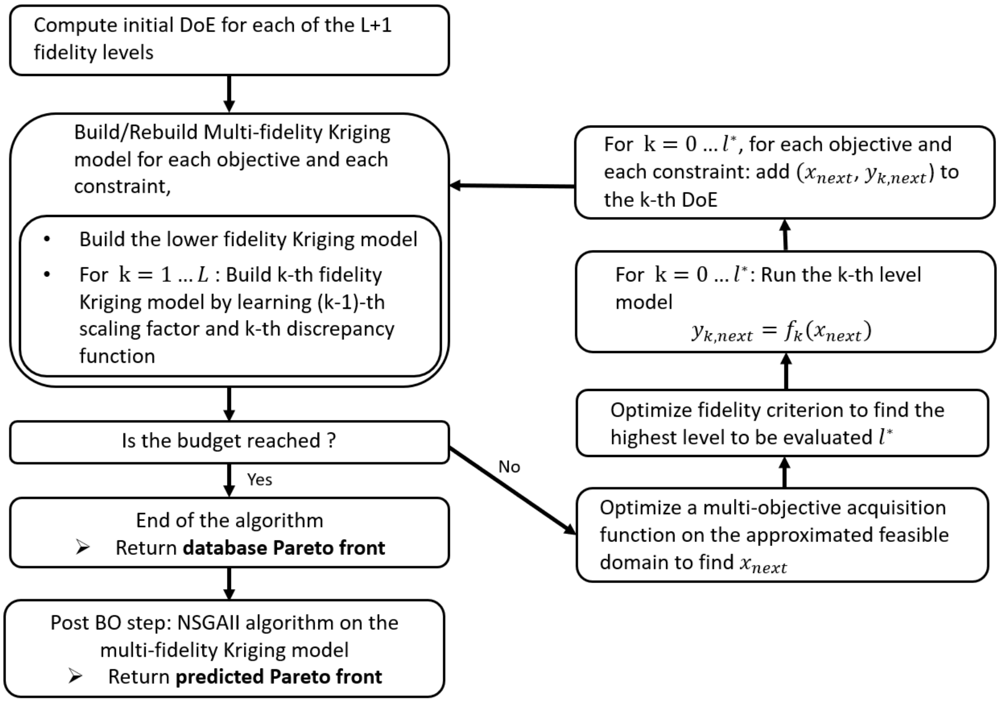

Figure 1: Diagram of the MFMO-SEGO methodology.

It is similar to the MFSEGO algorithm with four major differences. First a multi-fidelity Kriging model must be built for each of the objectives and constraints since we now deal with several objectives. Second, a multi-objective infill criterion must be used when solving the enrichment problem at each iteration. In this paper we used the multi-objective regularized infill criterion from [12] detailed in Eq.(9) with $\alpha_\mathbf{f}$ chosen as in Eq.(10) based on the MPI acquisition function. Third, some changes must be made to the level choice criterion. Indeed the criterion in Eq.(8) from Section 2.2 used in MFSEGO cannot be used anymore since the variance reduction is computed only for a single surrogate model. In the mono-objective case this single surrogate corresponds to the only objective, but in the multi-objective case, we need to take into account the variance reduction for each of the GP objective. The fourth difference comes at the end of the iteration process and consists of applying an evolutionary optimization algorithm like NSGAII [56] not directly to the expensive models but to the final multi-fidelity Kriging models (objectives and constraints). Since this latter optimization applies directly to the surrogate models, its cost is negligible compared to the cost of the iterative process that calls the expensive models multiple times. In the end we get a NSGAII predicted Pareto front and a database from which we can extract the database Pareto front. This post Bayesian optimization process step is referred as post-BO step in the following. Its goal is to derive a denser Pareto front than the database one and to use the behavior of the surrogate models to deduce areas of the Pareto front that are not necessarily represented in the database Pareto front. This is useful since Bayesian optimization alone is often performed with a small budget which not allows to populate a dense and complete Pareto front even if the surrogates capture well the behavior of the objective functions and constraints. Nevertheless, note that there is no guarantee that the predicted Pareto front will be actually accurate enough. Indeed, if the surrogate model is of poor accuracy, the same will probably be true for the predicted Pareto front.

For the level choice criterion modification, an extension of Eq.(8) has been proposed. The strategy is to compute for each objective the fidelity level l_o^* with which to evaluate the point as if we had several mono-objective problems. We choose l^* to be the maximum for all $o = 1, ..., n_{obj}$ of the l_o^*

$$l^* = \max\{l_1^*, ..., l_o^*, ..., l_{n_{obj}^*}\} \tag{12}$$

where

$$\forall o = 1, ..., n_{obj}, \quad l_o^* = \underset{l \in 0,...,L}{\arg\max} \; \frac{\sigma^2_{red,o}(l, x^*)}{(\sum_{i=0}^{l} c_{i,o})^2} \tag{13}$$

with $\sigma^2_{red,o}(l, x^*)$ being the variance reduction of the o-th objective surrogate model at point x^* using fidelity level l and $c_{i,o}$ being the associated cost.

Note that Eq.(12) relative to the maximization step could lead to enrich all objectives at a high fidelity level while it would be useful only for one of the objectives.

4. Understanding the performance of MFMO-SEGO

The MFMO-SEGO methodology from Section 3.2 has been assessed on four analytical test cases: ZDT1, ZDT2, ZDT3 and DTLZ5 problems in 6-dimension ($d = 6$). The optimization problems that we want to solve in this analytical test case section are of the following form:

$$x^* = \underset{x\in[0;1]^6}{\arg\min}[f_1^{HF}(x), f_2^{HF}(x)]^T \tag{14}$$
$$\text{such that} \quad \mathbf{g_i}^{HF}(x) \leq 0$$

These analytical test cases aim to validate the methodology before moving to a more realistic drone design problem.

4.1. Problems description

The three ZDT problems (see Table A.9 in Appendix A) are unconstrained problems in dimension 6 with two fidelity levels. They have been chosen in order to verify that our methodology could tackle different kinds of Pareto fronts. Indeed the ZDT1 analytical Pareto front is convex while the ZDT2 one is concave and the ZDT3 is discontinuous. The DTLZ5 problem, which is also in dmension 6 (see Table A.9 in Appendix A), has been augmented with a constraint to check that our method is capable of handling constrained multi-objective problems. It also has two fidelity levels. For the ZDT problems, the high fidelity objective function f_2^{HF} is of the form $f_2^{HF}(x) = u(x)v(f_1^{HF}(x), u(x))$. For all of the analytical problems, Table A.9 in Appendix A sums up the expressions of the high fidelity objective functions $f_1^{HF}(x)$, $f_2^{HF}(x)$ and the constraint while Table A.10 in Appendix A gives the expression of $u(x)$ and $v(x)$, two useful functions to construct the objective functions. In a multi-fidelity framework, the optimization is assisted by one or more low-fidelity functions. Here we consider two fidelity problems. Table A.11 in Appendix A sums up the expressions of the low fidelity functions $f_1^{LF}(x)$ and $f_2^{LF}(x)$ and the associated constraint for all of the analytical test cases.

4.2. Experimental setup

For each test case we made 10 mono fidelity optimization runs and 10 multi-fidelity ones varying the initial DoE. For the multi-fidelity runs we considered nested DoEs as explained in Section 2.1. To build these nested DoEs, we used latin hypercube sampling (LHS) [57] using the SMT toolbox [42, 58]. SMT can construct LHS thanks to different methods, in this paper we used the Enhanced Stochastic Evolutionary algorithm (ESE) [59]. To perform the optimization, we used the Super Efficient Global Optimization with Mixture Of Experts (SEGOMOE) framework developed between ONERA and ISAE-SUPAERO [60, 33, 34, 47].

Since the number of design variables is relatively high in our problems it is useful to use a dimension reduction technique in order to better solve the hyperparameters estimation based on likelihood maximization. Each analytical test case uses the MFKPLS dimension reduction technique described in Section 2.1 with the same truncated latent space dimension equals to 2. The surrogate models have been built with SMT [42] with a constant trend and a square exponential kernel.

The initial DoE sizes for the analytical test cases are summarized in Table 1. Using an initial HF DoE size equals to around three times the number of latent variables seems to be a good choice. For each run, the mono-fidelity initial DoE and the HF initial DoE are identical. Since the quality of the initial DoE has an impact on the convergence speed, this allows to compare legitimately the mono and multi-fidelity Bayesian optimization efficiencies. The budget allowed to the optimization algorithm for each analytical test case is detailed in Table 2, where the unit for the budget corresponds to the cost of one HF evaluation. We chose different budgets for each test case since they are more or less difficult to solve. Indeed, budgets are chosen so that the predicted Pareto fronts obtained using the multi-fidelity approach converge (mean of the IGD metric < 0.1).

Table 1: Initial DoE size for each analytical test case.

	ZDT1	ZDT2	ZDT3	DTLZ5
Initial HF DoE	6	6	6	6
Initial LF DoE	12	12	12	12

For the analytical test cases, the cost ratios between the high and low fidelity levels have been set to 100.

Table 2: Bayesian optimization budget, problem dimension and latent space dimension for the analytical test cases. One unit is equivalent to the cost of a HF evaluation.

	ZDT1	ZDT2	ZDT3	DTLZ5
Budget	6	12	20	10
Problem dimension	6	6	6	6
Latent space dimension	2	2	2	2

4.3. Performance metrics

Three performance metrics have been used to assess the performance of the MO-SEGO and MFMO-SEGO algorithms on all of the test cases: the hypervolume, the inverted generational distance (IGD) and the inverted generational distance plus (IGD^+) [61]. The means over the 10 runs of the hypervolume, IGD and IGD^+ metrics are computed for both the predicted and database Pareto fronts and for the two MO-SEGO and MFMO-SEGO algorithms. We call database Pareto front the Pareto front that we got at the end of the iterative process, before applying NSGAII to the final surrogate models. In parallel, the predicted Pareto front refers to the Pareto front obtained after applying NSGAII to the end of iterative process surrogate models. Note that the hypervolume metric computes a departure from a reference point while the IGD and IGD^+ metrics compute a departure from the reference Pareto front. Hence we search for the largest hypervolume and for the smaller IGD and IGD^+ values (ie the smaller departure from the reference Pareto front). The reference point used for the hypervolume computation could depend on the test case. For all of the analytical test cases, we chose the same reference point $R = (1.2, 1.2)$. The hypervolume metric has some limitations as it is possible, due to a bad prediction capability of the surrogate models that the predicted Pareto front dominates the reference Pareto front. Then the predicted Pareto front will have a larger hypervolume than the reference one. In this case, the hypervolume metric can not tell if the predicted Pareto front is better thanks to a good optimization or because of a bad prediction. On the other hand IGD computes a departure from the reference Pareto front so it does not suffer of this limitation. The counterpart is that to compute IGD we need a reference Pareto front not required for the hypervolume. Moreover the IGD metric is not weakly Pareto compliant. The IGD^+ metric uses a modified distance in order to ensure the weak Pareto compliancy property. But using this modified distance comes at the cost of suffering of the same kind of limitation as the hypervolume indicator in the sense that if the predicted Pareto front dominates the reference Pareto front due to bad prediction capabilities, these two fronts will have the same IGD^+ value equals to zero. It can be noted that the predicted Pareto front can not have a lower IGD^+ value than the reference Pareto front, even if it dominates the latter. After analysing the pros and cons of each of these indicators, we give more importance to the IGD metric as our method uses a prediction step. Remark that if we are not confident in the predicted Pareto front we can still evaluate some points of the predicted Pareto front in order to check if they really belong to the Pareto Front. As the solutions are known analytically (see Appendix A), the algorithm results will be compared to the reference solutions. The reference Pareto front is obtained by applying the HF objective functions to the reference Pareto set.

4.4. Numerical results

Table 3 summarizes the IGD performance metric values of the MO-SEGO and MFMO-SEGO algorithms on the analytical test cases. Table D.12 and Table D.13 sum up the performances respectively using the hypervolume and IGD^+ indicators. As the reference Pareto set is known, we applied to it the HF and the LF model to compare the values in the objective space with the ones of the mono and multi-fidelity optimization. Figures 2a and 3a show, respectively for the ZDT2 and ZDT3 problems, the reference Pareto front, the outputs of the LF model applied to the reference Pareto set points and the mono and multi-fidelity predicted Pareto fronts obtained using MO-SEGO and MFMO-SEGO algorithms. Next, respectively for the ZDT2 and ZDT3 and problems, the mono-fidelity database Pareto fronts obtained using MO-SEGO algorithms are depicted on Fig. 2b and 3b while the multi-fidelity database Pareto fronts obtained using MFMO-SEGO are on Fig. 2c and 3c. The figures relating to the ZDT1 and DTLZ5 problems are available in Appendix C.

The predicted Pareto fronts are closer to the reference solution than the database Pareto front for all analytic test cases, regardless of the metric we evaluate (hypervolume, IGD, or IGD^+), and regardless of the number of fidelity levels used in the optimizations. This highlights the usefulness of the NSGAII optimization performed on the surrogate models obtained at the end of the SEGOMOE iterative process. Analysis of the database Pareto fronts reveals that points on the extremes of the front are often added during BO last iterations (green color dots). For every test case, the database Pareto fronts obtained using multi-fidelity optimizations are better than the ones

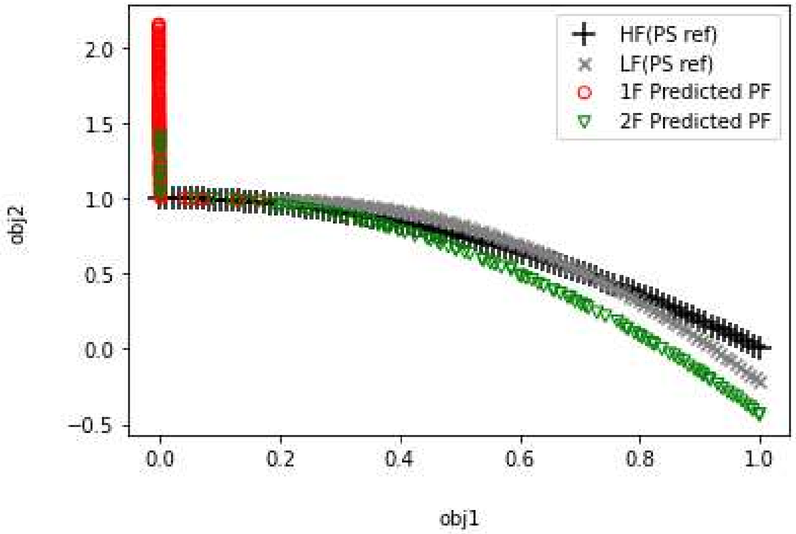

(a) 1F (mono-fidelity) and 2F (multi-fidelity) predicted Pareto front compared to the reference ones

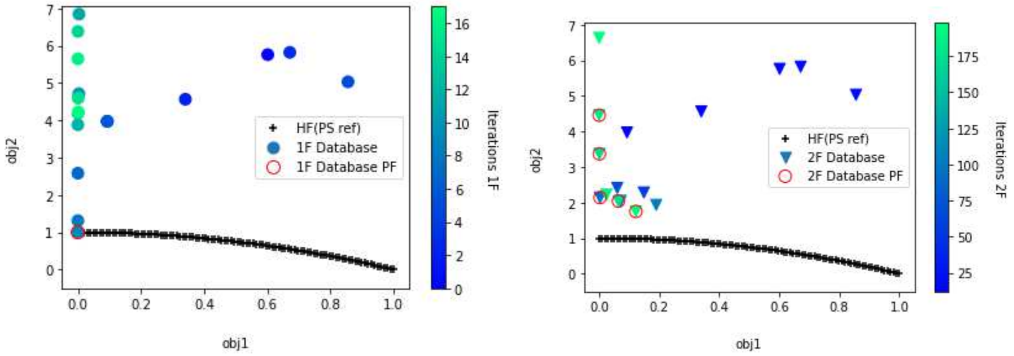

(b) 1F (mono-fidelity) optimization

(c) 2F (multi-fidelity) optimization

Figure 2: 2F (multi-fidelity) predicted Pareto front outperforms 1F (mono-fidelity) predicted Pareto front (a) (IGD value divided by 7.51 on this specific run and by 2.81 in average) and 2F (multi-fidelity) database Pareto front (c) underperforms 1F (mono-fidelity) database Pareto front (b) (IGD value multiplied by 1.91 on this specific run and by 1.83 in average), illustration on one of the ten ZDT2 runs. (For interpretation of the colors in the figure(s), the reader is referred to the web version of this article.)

obtained with mono-fidelity optimizations whatever the metric checked is, except for ZDT2. Still, the ZDT2 predicted Pareto fronts outputted by the multi-fidelity strategy are better than the ones from the mono-fidelity

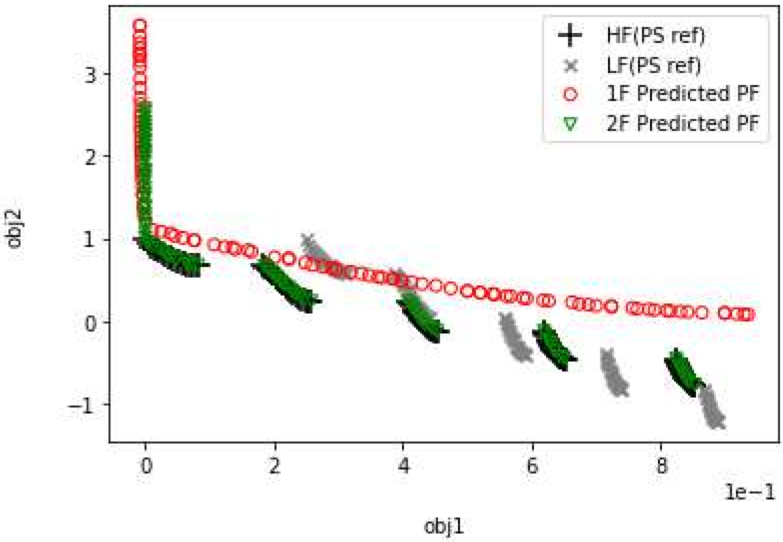

(a) 1F (mono-fidelity) and 2F (multi-fidelity) predicted Pareto front compared to the reference ones

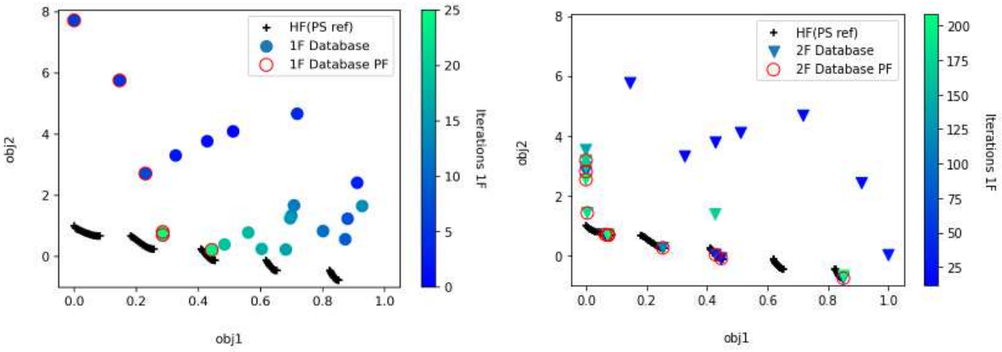

(b) 1F (mono-fidelity) optimization

(c) 2F (multi-fidelity) optimization

Figure 3: 2F (multi-fidelity) predicted Pareto front outperforms 1F (mono-fidelity) predicted Pareto front (a) (IGD value divided by 44.97 on this specific run and by 7.64 in average) and 2F (multi-fidelity) database Pareto front (c) outperforms 1F (mono-fidelity) database Pareto front (b) (IGD value divided by 3.27 on this specific run and by 5.33 in average), illustration on one of the ten ZDT3 runs. (For interpretation of the colors in the figure(s), the reader is referred to the web version of this article.)

regarding every metrics. Hence, the NSGAII run on the final surrogate model during the post-BO step seems to be even more interesting in a multi-fidelity context. For all the test cases, the predicted Pareto fronts from multi-fidelity

Table 3: Mean and standard deviation (between parenthesis) of the IGD metric for analytical test cases over the 10 runs. The lowest values are indicated in bold.

	ZDT1	ZDT2	ZDT3	DTLZ5
Reference Pareto front	0	0	0	0
MO-SEGO database	0.3755 (0.2075)	0.4148 (0.1900)	0.9058 (0.6297)	0.2653 (0.0836)
MO-SEGO predicted	0.1177 (0.1235)	0.1693 (0.2335)	0.7166 (0.5301)	0.1050 (0.0748)
MFMO-SEGO database	0.2214 (0.0829)	0.7611 (0.4344)	0.1698 (0.0700)	0.0809 (0.0347)
MFMO-SEGO predicted	**0.0154** (0.0075)	**0.0603** (0.0629)	**0.0938** (0.0639)	**0.0046** (0.0019)

optimizations are closer to the reference analytical Pareto front than the ones from mono-fidelity optimizations. Indeed the use of multi-fidelity allows to respectively divide the predicted Pareto front IGD value by a factor 7.64, 2.81, 7.64 and 22.82 for the ZDT1, ZDT2, ZDT3 and DTLZ5 problems as seen in Table 3. The same conclusions can be drawn from the two other performance indicators (see Appendix D). Interpreting the hypervolume and IGD^+ metrics is less straightforward. Regarding the ZDT2 problem (Table 3 and Fig. 2a), the predicted Pareto front hypervolume mean obtained from the multi-fidelity strategy is larger than the reference Pareto front hypervolume. One possible explanation is that the final surrogate models used by NSGAII at the end of the iterative process may have limited predictive accuracy and underestimate some objectives that need to be minimized. The predicted Pareto front could then lie below the reference Pareto front. On Fig. 2a, the grey curve, representing the LF reference Pareto set evaluations, plunges on its right side compared to the black curve, representing the HF reference Pareto set evaluations. Since the multi-fidelity surrogate models are partly driven by the LF function, this explains why the predicted Pareto front from the multi-fidelity strategy also plunges on the right side. However, IGD indicator cannot be misled by a falsely predicted Pareto front that would dominate the actual reference Pareto front. Therefore, we can still conclude that the multi-fidelity strategy overtakes the mono-fidelity approach even on the ZDT2 test case. In fact, the final mono-fidelity surrogate models may have even more limited predictive capabilities than the multi-fidelity ones and overestimate some objectives to minimize instead of underestimating them.

5. MDO of an electric drone

The MFMO-SEGO methodology has also been evaluated on a multi-fidelity and multi-objective fixed-wing electric drone optimization test case, considering an operation in the specific category: inspecting given positions of a high voltage line. The objectives and constraints of this optimization problem are calculated using electric drone models that have been developed to compute these quantities of interest, among others. Electric propulsion is attractive for drones [62, 63, 64, 65, 66]. In fact, it has a number of benefits, including reduced noise, a small thermal footprint, and the potential to be a carbon-free energy source (depending on the energy mix). However, it also has some drawbacks, including endurance, which may be overcome by combining it with fuel cells [64, 67, 68, 69]. This endurance drawback is also attenuated by our choice to design fixed-wing aircraft drones which are known for their ability to cover larger distances. In this section the developed electric drone models are described as well as the optimization problem.

5.1. The drone model

For the purpose of this work, two fixed-wing drone models have been developed: a high fidelity model (built upon medium fidelity disciplinary modules) and a low fidelity one. Both of them couple different disciplines (aerodynamic, structure, masses, geometry, mission, electric propulsion, cost) which are computed more or less accurately. The models take as inputs geometrical, structural, efficiency, manufacturing or battery variables. It outputs a lot of quantities of interest like: the final state of charge of the drone's battery (SOC) at the end of a specific mission (defined as a succession of checkpoints the drone must pass by), the maximal range the drone can cross using 75% of the battery making loops on the specified mission, the drone financial cost, the structural failure constraints and the mass of every lifting surfaces (wing and tail), the mission time, ... The models have been developed in Python using OpenMDAO, an open source MDO framework [70] from NASA Glenn and DYMOS [71], a framework for the simulation and optimization of dynamical systems within the OpenMDAO environment. The Extended Design Structure matrix (XDSM) [9] diagrams of our OpenMDAO analyses have been made thanks to WhatsOpt [72] which is a web application developed at ONERA to define and share multi-disciplinary analyses in terms of disciplines and data exchange. The aerostructural discipline relies on a tool called OpenAeroStruct (OAS) [73, 74, 75] developed by NASA and the University of Michigan. It is an open source lightweight tool that performs aerostructural analysis and optimization using OpenMDAO. It couples a vortex-lattice method (VLM) and a 6 degree of freedom 3-dimensional spatial beam model to simulate aerodynamic and structural analyses using lifting surfaces. To deal with the mission in the multi-disciplinary process, the low fidelity model relies on the electric Breguet range equation while the high fidelity model requires to solve an optimal control problem which is tackled using DYMOS. These two models are direct improvements of the drone models that we developed in previous work (see [16]). The additions made to these models concern the drone cost which is now modeled and the battery characteristics which now depend on a design variable and are not entirely fixed anymore. The low and high fidelity drone models are briefly described in Section 5.1.1 and Section 5.1.2 that focus on the new developments made on these models for the purpose of this work. To get more details about the LF and HF drone models, especially on the trajectory optimal control, please refer to our previous work [16].

5.1.1. Low fidelity electric drone model

Figure 4 depicts the LF model workflow with the different disciplinary modules. Regarding performance during mission computation, this model relies on an adaptation of the Breguet range equation to electric aircraft. The electric adaptation is given by:

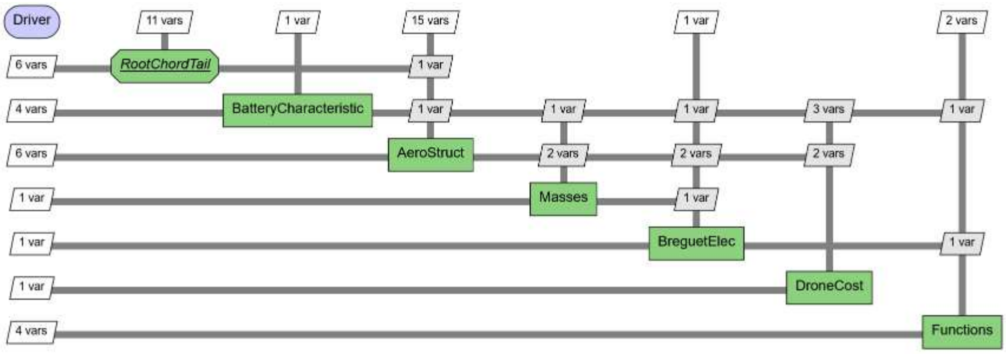

Figure 4: XDSM for the low fidelity drone model with the different disciplinary modules involved.

$$RangeMax = \frac{C_L}{C_D}\eta_p\eta_m\eta_{ESC}\frac{e_b}{g}\frac{m_{\text{batt}}}{m} \tag{15}$$

with η_p, η_m and η_{ESC} being respectively the efficiency coefficients for the propeller, the motor and the electronic speed controller. e_b is the battery specific energy, g the gravitational acceleration, m_{batt} the battery mass, and m is the total mass of the aircraft. This equation is valid in the steady level flight case. The low fidelity workflow is therefore the following. First, the RootChordTail sub-analysis balances the tail root chord in order to ensure longitudinal stability for the drone. Next, the battery characteristics like its mass, capacity, tension, maximal power and battery specific energy are deduced from the battery variables. The battery capacity is fixed to $15Ah.kg^{-1}$. The maximal battery power depends on the battery power per kg which is set to $3000W.kg^{-1}$. The battery tension depends on the chosen number of battery blocks of $3.7V$ and $5kg$ each. The battery block number is allowed to be continuous even if in practical life it must be discrete. Afterwards, the aerostructure component uses an OpenAeroStruct call to compute the lift and drag coefficients (the flight point used in the aerostructure component considers a 5 degree angle of attack and a speed of 20 ms^{-1}), the wing and tail failure values and the wing and tail masses which are passed to the masses component which deduces the overall drone mass. Then the electric Breguet range equation is applied to find the maximum range and the functions component is used to make approximation of the SOC at the end of the mission and of the maximal range using 75% of the battery. In this work the main improvement made to the previously developed [16] drone models is the drone cost model module. It is split in four different parts: the battery cost C_{batt}, the electric engine cost C_{motor}, the material cost C_{mat} and the manufacturing cost C_{mfg}. Others important cost areas of the drone like engineering, flight test operations, quality control or business support functions are not modelled here since we consider that the cost of these areas will not vary a lot depending on the chosen drone design. Each part of the cost model is detailed here.

Battery cost: The battery cost is a simple multiplication between the battery capacity in term of energy quantity (J) and the price of a lithium-ion battery per kWh.

$$\begin{aligned} C_{batt} &= capa_{batt}^{Qengy} \times C_{batt}^{perkWh} \times 3600 \times 1000 \quad (16) \\ &= (capa_{batt}^{Qcharge} \times tension_{batt}) \times C_{batt}^{perkWh} \times 3600 \times 1000 \quad (17) \end{aligned}$$

where $capa_{batt}^{Qengy}$ represents the battery capacity in term of energy quantity (J), $capa_{batt}^{Qcharge}$ represents the battery capacity in term of electric charge quantity (Coulomb) and $tension_{batt}$ represents the battery tension (Volt). We multiply by 3600×1000 to convert J in kWh. The battery cost per kWh is chosen to be equal to 150€$/kWh$ since it is approximately the early 2023 cost of an overall Li-ion battery pack per kWh.

Electric motor cost: The cost of the electric engine is a multiplication between the output power of the motor and the price of such an electric engine per kW.

$$\begin{aligned} C_{motor} &= P_{motor} \times \frac{C_{motor}^{perkW}}{1000} && (18) \\ &= (mass_{batt} \times P_{batt}^{perkg} \times \eta_{ESC} \times \eta_{motor}) \times \frac{C_{motor}^{perkW}}{1000} && (19) \end{aligned}$$

where P_{motor} represents the output power of the electric engine (Watt). C_{motor}^{perkW} represents the approximated cost of an electric engine per kW it is chosen to be equal to 150€$/kW$ as in [76]. $mass_{batt}$ represents the battery mass carried by the drone. P_{batt}^{perkg} represents the battery power per kilogram. η_{motor} and η_{ESC} are respectively the motor and electric speed controller efficiency coefficients. We divide by 1000 to convert W in kWh.

Material cost: The cost of the material is a multiplication between the airframe mass obtained from the drone structural model and the price of carbon fiber per kilogram

$$C_{mat} = mass_{airframe} \times C_{carbon}^{perkg} \quad (20)$$

where C_{carbon}^{perkg} represents the approximated cost of aeronautical carbon fiber per kg. We fixed it to 16€$/kg$ which is the current price of carbon fiber. $mass_{airframe}$ represents the airframe mass of the drone in kilogram.

Manufacturng cost: The cost of the manufacturing is a multiplication between the needed manufacturing hours and the labour cost of a manufacturing hour

$$C_{mfg} = h_{mfg} \times r_{mfg} \times infl_{19-23} \tag{21}$$

where r_{mfg} represents the labour cost of a manufacturing hour. In France according to the INSEE (french National Institute of Statistic and Economical Studies), the 2019 average gross salary of a qualified worker is of 32900€ per year. The legal number of hours worked by a full time employee is $1607h$ and we can approach the employer's charges to 25% of the gross salary, which leads to choose $r_{mfg} = \frac{1.25\times32900}{1607} = 25.59€/h$. $infl_{19-23} = 1.16$ is the value of the inflation between december 2019 (year of the data from INSEE) and january 2023 (year of this document). Its value has been obtained thanks to the US Bureau of Labor Statistics CPI inflation calculator. h_{mfg} represents the approximated number of manufacturing hours needed to build the drone.

$$\begin{aligned} h_{mfg} = 7.37 mass_{airframe}^{0.82} \times vmax_{lf}^{0.484} \times n_{drone} \times flap_{coeff} \\ \times (1 + 0.25 f_{comp}) \times F_{exp}^{1.4427 ln(n_{drone})} \times (1 + 0.25 f_{hyb}) \end{aligned} \tag{22}$$

To compute h_{mfg} we used Eq.(22) data driven model from [76]. Table 4 defines and set the input values of Eq.(22) manufacturing hours model. Typically, $F_{exp} \in [0.8, 1]$. In the LF model we suppose that we do not have any information on the F_{exp} value, so we set it to 0.9, the central value of its living interval.

Table 4: Input values of the manufacturing hours model definition.

Variable	description	Value	Unit
$vmax_{lf}$	Maximal speed at level flight	50	m/s
n_{drone}	Number of drone to build	1	$\emptyset$
$flap_{coeff}$	Coeff to take into account the flap construction difficulty	1	$\emptyset$
f_{comp}	Proportion of composite material used	1	$\emptyset$
F_{exp}	Experience effectiveness factor	0.85 (HF) or 0.9 (LF)	$\emptyset$
f_{hyb}	Proportion of hybrid propulsion system	1	$\emptyset$

5.1.2. High fidelity electric drone model

The HF drone model takes the mission the drone must perform into account more precisely than the LF model. This mission is defined by some control points the drone must pass by and the HF model computes the optimal trajectory in term of energy consumption allowing to respect the mission definition, i.e.: to pass through the waypoints. The optimal control problem is solved using DYMOS [71], the OpenMDAO package for optimal control. A constraint is added to the optimal control problem in order to ensure that the maximum possible thrust is not exceeded during the mission. In this work, the considered mission over which the model is evaluated is one of the specific missions tested in [16]. It consists in a climb phase, a cruise phase and a descent phase. An overview of this mission is available in Fig. B.9 in Appendix B. Figure 5 shows the XDSM diagram of the high fidelity drone model with the main disciplinary modules involved. The workflow of the high fidelity model is as follows. First, as with the low fidelity model, the tail root chord is balanced to ensure the longitudinal stability of the drone and the battery characteristics are computed. To do this, we used exactly the same modules as for the low-fidelity model. Next, we perform the structural sizing using a call to OpenAeroStruct at the most critical flight point (maximum speed and maximum angle of attack) since it is the flight point where the structure is most likely to break. This component computes the wing and tail failure constraints and the wing and tail masses. The same aerostructural description is used as in the LF model (same mesh, same material, same safety margin). Afterwards, the mission is completed by solving the optimal control problem using DYMOS instead of using the electric Breguet range equation as in the LF model. The corresponding component provides the mission time and the

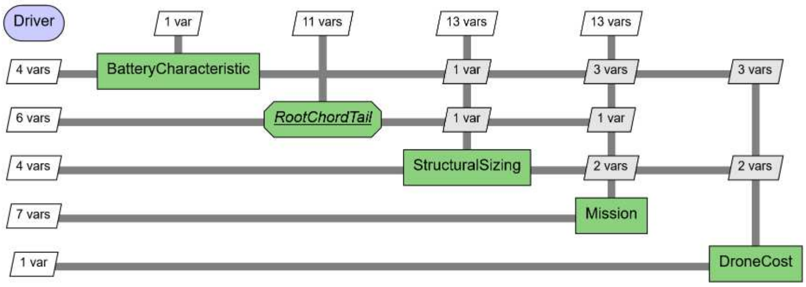

Figure 5: XDSM for the high fidelity drone model with the different disciplinary modules involved.

end of mission battery SOC. The maximal range the drone can cover using 75% of the battery and making loops over the specified mission is extrapolated from the end of mission SOC. Finally, the drone cost is evaluated in the same way as in the LF model except that for the HF model we consider that we have been able to evaluate the experience-related worker effectiveness parameter F_{exp}. It is estimated to 0.85 for all drone configurations. Table 5 summarizes the differences between the LF and the HF model.

Table 5: Differences between the LF and the HF model.

	LF	HF
Mission	Based on electric Breguet range equation	Solve an optimal control problem with DYMOS to perform the mission
Structural sizing	OAS call ($AoA = 5$ degrees, airspeed = 20 ms^{-1})	OAS call at the most critical flight point ($AoA = 15$ degrees, airspeed = 50 ms^{-1})
Drone cost model	$F_{exp} = 0.9$	$F_{exp} = 0.85$

5.2. Problem description

In the drone test case, the optimization problem that we aim to solve consists in minimizing simultaneously the drone cost and the opposite of the maximal range the drone can cover using 75% of the battery. This problem is constrained with two inequality structural constraints to ensure that neither the wing nor the tail fail during the flight. These constraints compare the Von Mises stress computed by OAS to the yield stress divided by a fixed coefficient. The yield stress depends on the material chosen for the structural spar. In our model we chose high modulus carbon fiber as material which leads to the following values [77]: Young modulus $E = 85e9\ Pa$, shear modulus $G = 25e9\ Pa$, material density of $1.6e3\ kgm^{-3}$ and yield stress equals to $350e6\ Pa$. The fixed coefficient acts as a safety margin and is chosen equal to 2.5. To compute failure constraints, OAS provides two methods. The most direct way to proceed is to check the Von Mises stress at each node of the mesh. But we used the other method that aggregates the individual nodal failure constraints using a Kreisselmeier-Steinhauser (KS) function [78]. The KS function produces a smoother constraint than using a max() function to find the maximum point of failure, which is useful to produce a better-posed optimization problem. For each surface (wing or tail) we have a constraint of the following form:

$$failure = f_{\max} + \frac{1}{p}\log(\Sigma_{i\in S}(\exp(p(\frac{\sigma_{vm,i}}{\frac{yield}{2.5}} - 1 - f_{\max})))) \leq 0 \tag{23}$$

with S being the set of mesh nodes for the associated lifting surface (wing or tail). $\sigma_{vm,i}$ is the Von Mises stress at the i-th node of S. We also define $f_{\max} = \max_{i\in S}\left(\frac{\sigma_{vm,i}}{\frac{yield}{2.5}}\right) - 1$. The p parameter controls how conservatively the KS function aggregates the failure constraints. A lower value is more conservative while a greater value is more aggressive (closer approximation to the max() function). We consider 20 design variables which are essentially wing and tail geometrical variables except for the number of battery blocks composing the drone battery. For this last variable, even if in practice it should be a discrete variable, in this work it is fully treated as a continuous one since our optimization methodology is not able to address integer variables yet. All the design variables are summarized in Table 6.

Finally, the optimization problem associated with the drone test case can be expressed as:

$$\begin{aligned} x^* = \; & \underset{x\in\Omega\subset\mathbb{R}^{20}}{\arg\min} \; [\text{DroneCost}^{HF}(x), -\text{RangeMax}^{HF}_{75\%}(x)]^T \\ & \text{such that} \begin{cases} \text{wing}_{\text{failure}}(x) \leq 0 \\ \text{tail}_{\text{failure}}(x) \leq 0 \end{cases} \end{aligned} \tag{24}$$

All the necessary quantities of interest for this problem can be computed using the drone models detailed in Section 5.1.

5.3. Experimental setup

The drone test case experimental setup is quite similar to the one of analytical test cases. The modifications considered for the Drone problem are detailed in Table 7.

To assess the cost ratio for the drone test case, 100 points (i.e. drone configurations) have been chosen randomly according to a uniform distribution within the design space. Then they have been computed to deduce both the CPU time mean values for HF and LF models. The deduced cost ratio between the two values is 116. Note that in order to take into account the nested DoE assumption, the cost of the HF model is considered as the sum of

Table 6: Definition of the 20 design variables.

variables	design space	unit	quantity
wing span	$[5, 6]$	m	1
root chord wing	$[1, 1.2]$	m	1
wing taper ratio	$[0.6, 1]$	no unit	1
wing sweep angle	$[0, 5]$	degree	1
tail sweep angle	$[0, 5]$	degree	1
wing dihedral angle	$[-3, 3]$	degree	1
tail dihedral angle	$[-3, 3]$	degree	1
structural tube thickness control points along wing span	$[0.001, 0.01]^3$	m	3
structural tube thickness control points along tail span	$[0.001, 0.01]^3$	m	3
twist control points along wing span	$[1, 1.5] \times [0.5, 1] \times [0, 0.5]$	degree	3
twist control points along tail span	$[1, 1.5] \times [0.5, 1] \times [0, 0.5]$	degree	3
Number of battery blocks	$[2, 4]$		1
Total number of design variables			**20**

Table 7: Drone test case experimental setup.

HF init DoE size	10
LF init DoE size	20
BO budget	10
Input space dimension	20
Truncated latent space dimension	3
cost ratio	116

the cost of an LF evaluation and an HF evaluation. The drone problem solution is not known analytically. Then to get a reference solution to compare with, we ran the NSGAII algorithm with a budget of 2000 HF evaluations on the drone problem.

5.4. Discussion of numerical results

The same hypervolume, IGD and IGD^{+} performance metrics have been used to assess the performance of the MO-SEGO and MFMO-SEGO algorithms on this drone test case. A different reference point $R = (70000, 22000)$ has been chosen to evaluate the hypervolume for this problem. Table 8 summarizes the hypervolume, IGD and $IGD+$ values of the MO-SEGO and MFMO-SEGO algorithms for the drone test case. Figure 6a shows the reference Pareto front, the outputs of the LF model applied to all of the points from the reference Pareto set and the mono and multi-fidelity predicted Pareto fronts obtained using MO-SEGO and MFMO-SEGO algorithms. We can see that the LF model is significantly different from the HF model even if they have a comparable trend. Next Fig. 6b and 6c show, also for the drone problem, the mono and multi-fidelity database Pareto fronts obtained using MO-SEGO and MFMO-SEGO algorithms.

Table 8: Mean and standard deviation (between parenthesis) of the hypervolume, IGS and $IGD+$ metrics for the drone test case over the 10 runs. The closest best values are indicated in bold.

	Hypervolume	IGD	$IGD+$
Ref Pareto front	2.0141e9	0	0
MO-SEGO database Pareto front	1.0806e9 (111250596)	14340.81 (3072)	8374.15 (4556)
MO-SEGO predicted Pareto front	1.7274e9 (53339581)	2088.79 (960)	1728.31 (1033)
MFMO-SEGO database Pareto front	1.1618e9 (102595746)	12541.71 (2436)	4256.73 (2344)
MFMO-SEGO predicted Pareto front	**1.9833e9** (46231133)	**608.21** (172)	**137.18** (163)

This more realistic drone design optimization test case confirms the behaviors observed in the analytical ones. The predicted Pareto front outperforms the database Pareto front regardless of the number of fidelity levels used or the metric considered. The multi-fidelity optimization approach yields better database Pareto fronts compared to mono-fidelity optimization, and the predicted Pareto fronts from multi-fidelity optimization also outperform those from mono-fidelity optimization. Specifically, multi-fidelity optimization reduces the IGD value of the database Pareto front by a factor

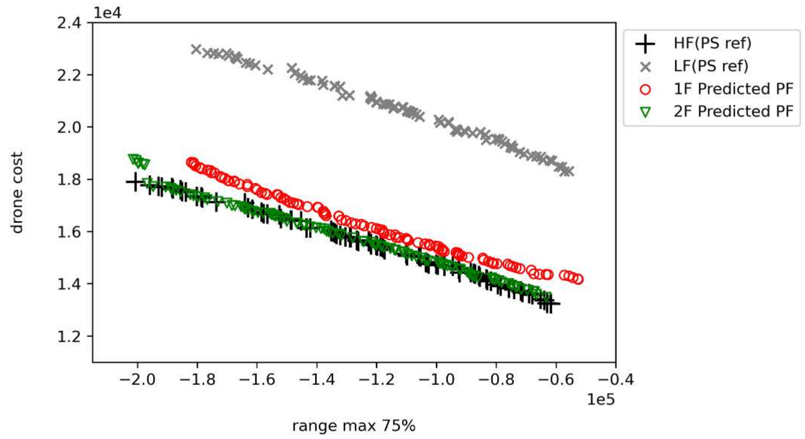

(a) 1F (mono-fidelity) and 2F (multi-fidelity) predicted Pareto front compared to the reference ones

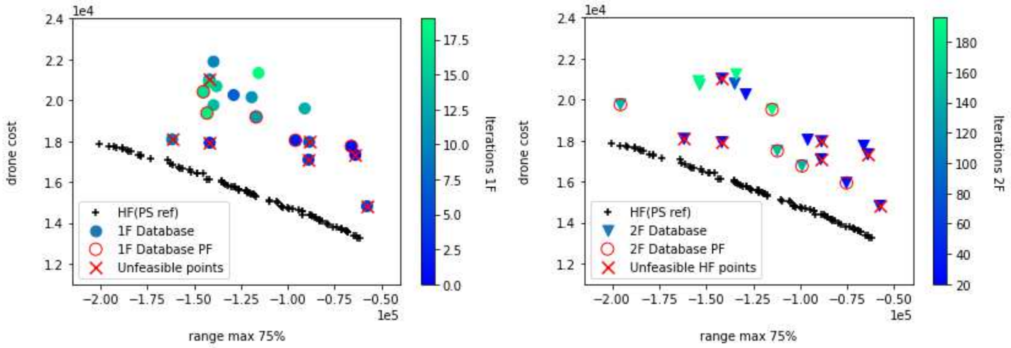

(b) 1F (mono-fidelity) optimization

(c) 2F (multi-fidelity) optimization

Figure 6: 2F (multi-fidelity) predicted Pareto front outperforms 1F (mono-fidelity) predicted Pareto front (a) (IGD value divided by 2.96 on this specific run and by 3.43 in average) and 2F (multi-fidelity) database Pareto front (c) outperforms 1F (mono-fidelity) database Pareto front (b) (IGD value divided by 1.05 on this specific run and by 1.14 in average), illustration on one of the ten drone runs. (For interpretation of the colors in the figure(s), the reader is referred to the web version of this article.)

of 1.14, the IGD^+ value by a factor of 1.97, and increases the hypervolume value by a factor of 1.08. Similarly, for the predicted Pareto front, multi-fidelity optimization reduces the IGD value by a factor of 3.43, the IGD^+ value by a factor of 12.60, and increases the hypervolume value by a factor of 1.15. Thus, the drone test case provides further evidence that the multi-fidelity methodology outperforms the mono-fidelity approach. As an indication, three noteworthy designs from the optimal predicted Pareto set of one of the ten multi-fidelity runs are described in Fig. 7. Their position on the corresponding predicted Pareto front can be visualized on Fig. 8. The first design (magenta dotted line) corresponds to a design that focuses on minimizing the drone cost, the second (orange dashed line) focuses on minimizing the opposite of the maximal achievable range while the third one (cyan solid line) is a compromise between both objectives. One can remark that the number of battery blocks variable is of great interest for both objectives. A bigger battery will increase maximal range but will also increase the drone cost. It is worth noting that some variables like the ones defining the tail design do not have a big impact on both objectives. This highlights that the use of a dimension reduction technique is a wised choice for our application.

6. Conclusion and perspectives

In this work, we proposed a multi-fidelity & multi-objective optimization algorithm based on Bayesian optimization. We evaluated the performance of this methodology with some comparisons to the mono-fidelity counterpart on analytical constrained or unconstrained problems in dimension 6. The results obtained on the four problems with different Pareto front characteristics such as convexity and continuity confirmed the effectiveness of the proposed strategy. We then applied both methodologies to a more realistic drone design problem in dimension 20 with two constraints. We improved the accuracy of the low-fidelity and high-fidelity drone models used in previous studies by including battery characteristics and financial cost computations. Our numerical results showed that the multi-fidelity & multi-objective MFMO-SEGO methodology outperforms the single-fidelity & multi-objective MO-SEGO methodology. This performance comparison holds either if we consider only the Bayesian optimization step of the method (database Pareto front) or if we consider both the Bayesian optimization step and the post-BO optimization of the surrogate model step using NSGAII (predicted Pareto front). Furthermore, our study highlights the significant improvements brought by the post-BO NSGAII surrogate model optimization step to the Pareto front. In future work, we plan to implement additional multi-objective fidelity level selection criteria to investigate whether we can achieve similar optimization results with less use of the high fidelity model. Moreover, it is also planned to investigate the use of an uncoupled multi-objective fidelity level selection cri-

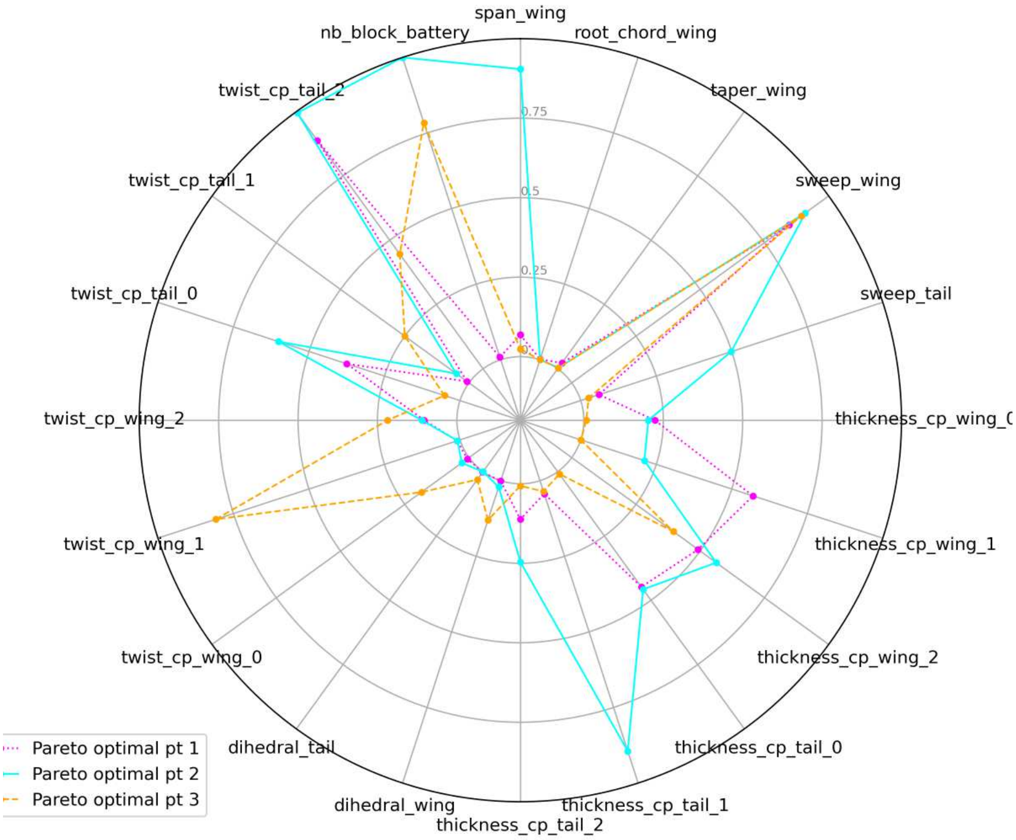

Figure 7: Radar plot of three noteworthy Pareto optimal designs. The first design (magenta dotted line) corresponds to a design that focuses on minimizing the drone cost, the second (cyan solid line) focuses on minimizing the opposite of the maximal achievable range while the third one (orange dashed line) is a compromise between both objectives.

terion by testing a configuration where each objective is given by a dedicated model. Finally, we aim to expand the algorithm's capabilities by coupling it with mixed variables Bayesian optimization techniques.

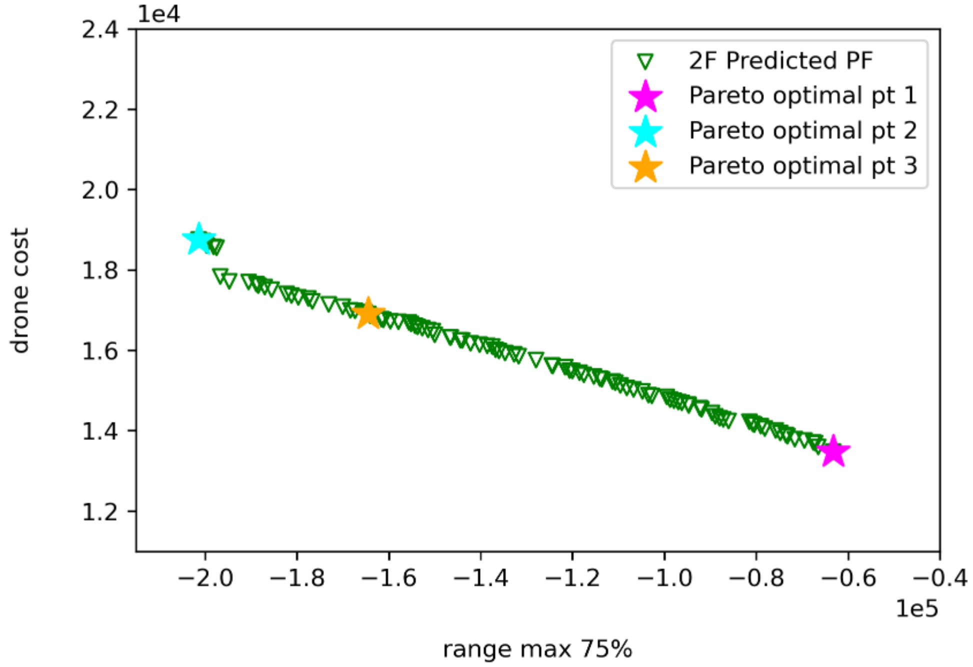

Figure 8: Positions on the predicted Pareto front of one of the ten multi-fidelity runs of three noteworthy Pareto optimal designs. The first design (magenta) corresponds to a design that focuses on minimizing the drone cost, the second (cyan) focuses on minimizing the opposite of the maximal achievable range while the third one (orange) is a compromise between both objectives.

Acknowledgments

The PhD is funded by the Defence Innovation Agency (AID) and by the French Directorate General of Armaments (DGA) as part of the CONCORDE research project (No 2019 65 0090004707501). This work is part of the activities of ONERA–ISAE–ENAC joint research group.

Appendix A. Analytical functions

The following tables describe the analytical functions used in this paper. Table A.9 shows the expressions of the high fidelity analytical objective functions and constraints. Table A.10 gathers the u and v function definitions for each test case. Table A.11 shows the expressions of the low fidelity analytical objective functions and constraints.

Table A.9: Expressions of the high fidelity analytical functions and constraint.

Problem	$f_1^{HF}(x) =$	$f_2^{HF}(x) =$	Constraint
ZDT1	x_1	$u(x)v(x)$	-
ZDT2	x_1	$u(x)v(x)$	-
ZDT3	x_1	$u(x)v(x)$	-
DTLZ5	$(1 + u(x_Q)) \cos(0.5\pi x_1)$	$(1 + u(x_Q)) \sin(0.5\pi x_1)$	$f_1^{HF}(x) \leq 0.5$

The ZDT1 optimal problem solution is given by the following Pareto set:

$$\{x \in \mathbb{R}^6, \quad (0 \leq x_1^* \leq 1) \quad \wedge \quad (x_i^* = 0 \;\; \text{for} \;\; i = 2, \ldots, 6)\}$$

The ZDT2 solution is given by the following Pareto set:

$$\{x \in \mathbb{R}^6, \quad (0 \leq x_1^* \leq 1) \quad \wedge \quad (x_i^* = 0 \;\; \text{for} \;\; i = 2, \ldots, 6)\}$$

The ZDT3 solution is given by the following Pareto set:

$$\{x \in \mathbb{R}^6, \quad (x_1^* \in [0, 0.083] \cup [0.1822, 0.2577] \cup [0.4093, 0.4538] \cup [0.6183, 0.6525] \\ \cup [0.8233, 0.8518]) \quad \wedge \quad (x_i^* = 0 \;\; \text{for} \;\; i = 2, \ldots, 6)\}$$

For the DTLZ5 test case, x_Q denotes the vector of the last $(d - n_{obj} + 1)$ design variables. For example, if $d = 6$, $n_{obj} = 2$, then x_Q will be the vector of the last five design variables in x. The constraint used in the DTLZ5 problem consists in ensuring that the first HF objective is lower than or equal to 0.5: $f_1^{HF} \leq 0.5$. Considering this constraint we are still able to express the analytical Pareto set for this test case by restricting the unconstrained DTLZ5 Pareto set (given by $\{x \in [0, 1]^6, x_2 = x_3 = x_4 = x_5 = x_6 = 0.5\}$) to the points where $x_1 \leq 0.5$. Indeed, x_1 living in $[0, 1]$, $\cos(0.5\pi x_1) \leq 0.5 \Leftrightarrow x_1 \in [0, 0.5]$.

Appendix B. Mission overview

The following Fig. B.9 is an overview of the mission used in the drone design test case. This mission is the same as in [16].

Appendix C. Additional result figures

This section presents additional figures: Fig. C.10 for the ZDT1 test case and Fig. C.11 relative to DTLZ5 test case.

Table A.10: Expressions of functions g and h.

Problem	$u(x)$	$v(x)$
ZDT1	$1+\frac{9}{d-1}\sum_{i=2\ldots d} x_i$	$1-\sqrt{\frac{f_1^{HF}(x)}{u(x)}}$
ZDT2	$1+\frac{9}{d-1}\sum_{i=2\ldots d} x_i$	$1-(\frac{f_1^{HF}(x)}{u(x)})^2$
ZDT3	$1+\frac{9}{d-1}\sum_{i=2\ldots d} x_i$	$1-\sqrt{\frac{f_1^{HF}(x)}{u(x)}}-\frac{f_1^{HF}(x)}{u(x)}\sin(10\pi f_1^{HF}(x))$
DTLZ5	$\sum_{x_i\in x}(x_i-0.5)^2$	-

Table A.11: Expressions of the low fidelity analytical functions and constraint.

Problem	$f_1^{LF}(x)$	$f_2^{LF}(x)$	Constraint
ZDT1	$0.9x_1+0.1$	$(0.8u(x)-0.2)(1.2v(x)+0.2)$	-
ZDT2	$0.8x_1+0.2$	$(0.9u(x)+0.2)(1.1v(x)-0.2)$	-
ZDT3	$0.75x_1+0.25$	$u(x)(1.25v(x)-0.25)$	-
DTLZ5	$(1+0.8u(x_Q))\cos(0.5\pi x_1)$	$(1+1.1u(x_Q))\sin(0.5\pi x_1)$	$f_1^{LF}(x)\leq 0$

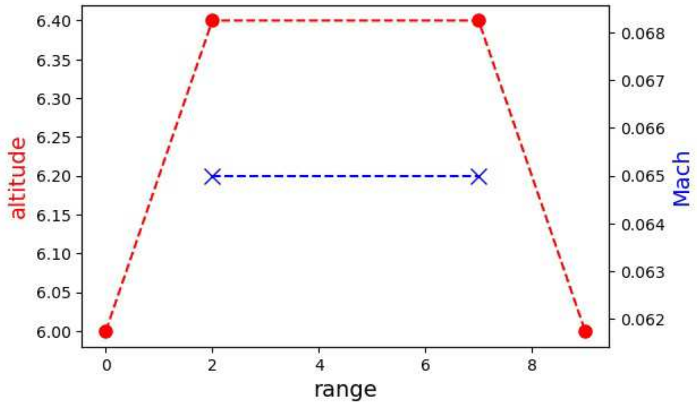

Figure B.9: Mission overview (4 control points)

Appendix D. Additional result tables

In this section we gather additional results for the analytical test cases (Table D.12 and Table D.13). These results concern the means of the hyper-

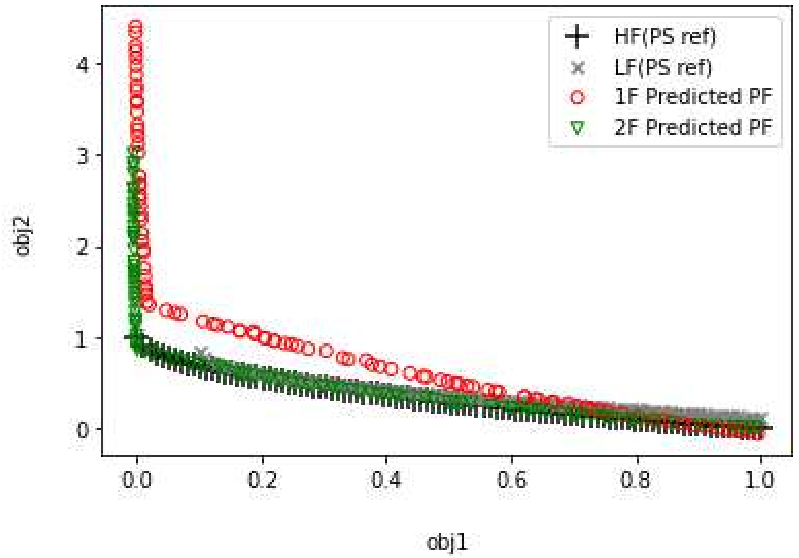

(a) 1F (mono-fidelity) and 2F (multi-fidelity) predicted Pareto front compared to the reference ones

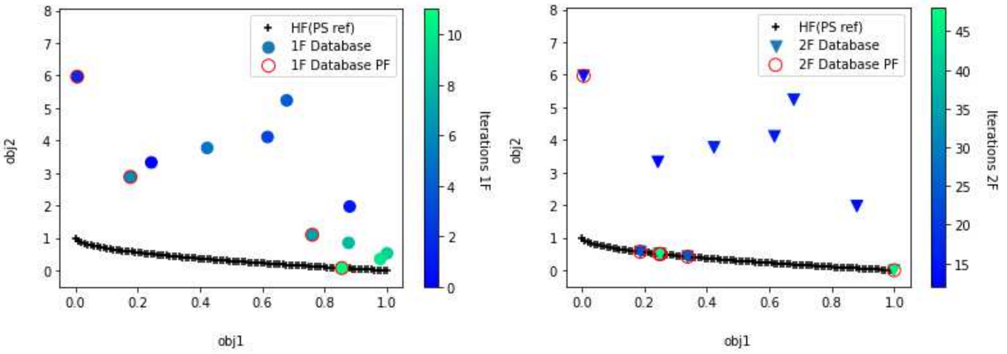

(b) 1F (mono-fidelity) optimization

(c) 2F (multi-fidelity) optimization

Figure C.10: 2F (multi-fidelity) predicted Pareto front outperforms 1F (mono-fidelity) predicted Pareto front (a) (IGD value divided by 13.05 on this specific run and by 7.64 in average) and 2F (multi-fidelity) database Pareto front (c) outperforms 1F (mono-fidelity) database Pareto front (b) (IGD value divided by 2.54 on this specific run and by 1.7 in average), illustration on one of the ten ZDT1 runs. (For interpretation of the colors in the figure(s), the reader is referred to the web version of this article.)

volume and IGD^+ metrics over the analytical test cases.

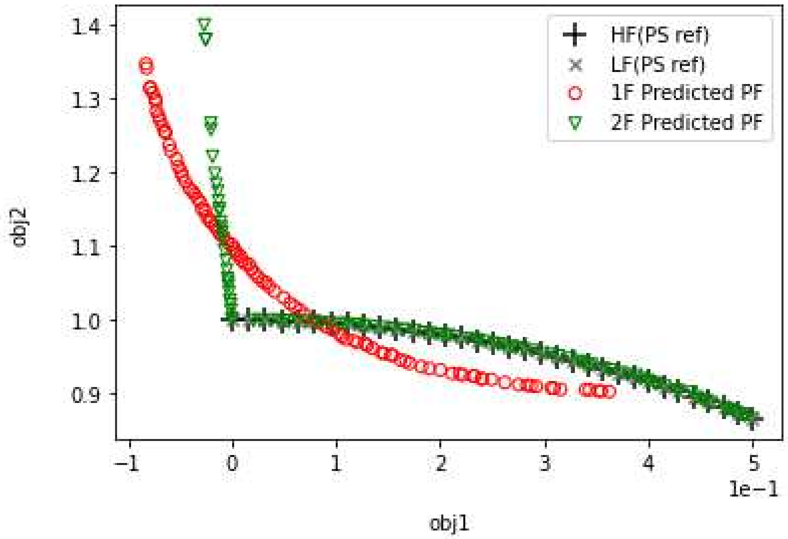

(a) 1F (mono-fidelity) and 2F (multi-fidelity) predicted Pareto front compared to the reference ones

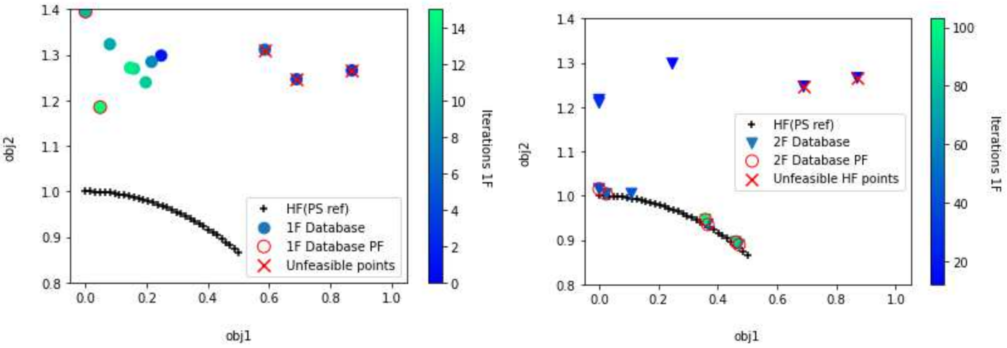

(b) 1F (mono-fidelity) optimization

(c) 2F (multi-fidelity) optimization

Figure C.11: 2F (multi-fidelity) predicted Pareto front outperforms 1F (mono-fidelity) predicted Pareto front (a) (*IGD* value divided by 23.06 on this specific run and by 22.82 in average) and 2F (multi-fidelity) database Pareto front (c) outperforms 1F (mono-fidelity) database Pareto front (b) (*IGD* value divided by 5.28 on this specific run and by 3.28 in average), illustration on one of the ten DTLZ5 runs. (For interpretation of the colors in the figure(s), the reader is referred to the web version of this article.)

Table D.12: Mean and standard deviation (between parenthesis) of the hypervolume metric for analytical test cases over the 10 runs. The closest values to the reference hypervolume values are indicated in bold.

	ZDT1	ZDT2	ZDT3	DTLZ5
Reference Pareto front	1.1014	0.7683	1.6365	0.3545
MO-SEGO database Pareto front	0.6012 (0.2358)	0.3820 (0.0.1306)	0.5457 (0.3926)	0.1335 (0.1004)
MO-SEGO predicted Pareto front	1.0395 (0.2177)	0.5920 (0.2277)	0.6845 (0.4291)	0.3900 (0.0856)
MFMO-SEGO database Pareto front	0.8230 (0.0650)	0.2085 (0.2330)	1.4082 (0.1340)	0.2896 (0.0315)
MFMO-SEGO predicted Pareto front	**1.0932** (0.0209)	**0.8456** (0.1719)	**1.4628** (0.1063)	**0.3496** (0.0066)

Table D.13: Mean and standard deviation (between parenthesis) of the IGD^+ metric for analytical test cases over the 10 runs. The lowest values are indicated in bold.

	ZDT1	ZDT2	ZDT3	DTLZ5
Reference Pareto front	0	0	0	0
MO-SEGO database	0.2742 (0.1896)	0.2339 (0.1191)	0.8470 (0.6482)	0.1387 (0.0809)
MO-SEGO predicted	0.0666 (0.0714)	0.1107 (0.1445)	0.6848 (0.5346)	0.0120 (0.173)
MFMO-SEGO database	0.1374 (0.0429)	0.6493 (0.4508)	0.0942 (0.0651)	0.0350 (0.0181)
MFMO-SEGO predicted	**0.0081** (0.0067)	**0.0211** (0.0495)	**0.0763** (0.0527)	**0.0030** (0.0017)

References

[1] S. S. Baek, H. Kwon, J. A. Yoder, D. Pack, Optimal path planning of a target-following fixed-wing uav using sequential decision processes, in: 2013 IEEE/RSJ International conference on intelligent robots and systems, IEEE, 2013, pp. 2955–2962.

[2] S.-L. Liao, R.-M. Zhu, N.-Q. Wu, T. A. Shaikh, M. Sharaf, A. M. Mostafa, Path planning for moving target tracking by fixed-wing uav, Defence Technology 16 (4) (2020) 811–824.

[3] D. A. Flores, C. Saito, J. A. Paredes, F. Trujillano, Multispectral imaging of crops in the peruvian highlands through a fixed-wing uav system, in: 2017 IEEE International Conference on Mechatronics (ICM), IEEE, 2017, pp. 399–403.

[4] M. Hakim, H. Pratiwi, A. Nugraha, S. Yatmono, A. Wardhana, E. Damarwan, T. Agustianto, S. Noperi, Development of unmanned aerial vehicle (uav) fixed-wing for monitoring, mapping and dropping applications on agricultural land, in: Journal of Physics: Conference Series, Vol. 2111, IOP Publishing, 2021, p. 012051.

[5] T. Templin, D. Popielarczyk, R. Kosecki, Application of low-cost fixed-wing uav for inland lakes shoreline investigation, Pure and Applied Geophysics 175 (2018) 3263–3283.

[6] M. Mulero-Pázmány, J. R. Martínez-de Dios, A. G. Popa-Lisseanu, R. J. Gray, F. Alarcón, C. A. Sánchez-Bedoya, A. Viguria, C. Ibáñez, J. J. Negro, A. Ollero, et al., Development of a fixed-wing drone system for aerial insect sampling, Drones 6 (8) (2022) 189.

[7] W. Yi, C. Liming, K. Lingyu, Z. Jie, W. Miao, Research on application mode of large fixed-wing uav system on overhead transmission line, in: 2017 IEEE International Conference on Unmanned Systems (ICUS), IEEE, 2017, pp. 88–91.

[8] C. Vidan, S. Pop, Interpretation of flight data from a fixed-wing uav system dedicated to flying over high voltage lines, INCAS Bulletin 14 (2) (2022) 121–128.

[9] J. R. R. A. Martins, A. Ning, Engineering design optimization, Cambridge University Press, 2021.

[10] P. I. Frazier, A tutorial on Bayesian optimization, arXiv preprint arXiv:1807.02811 (2018).

[11] M. Saporito, A. Da Ronch, N. Bartoli, S. Defoort, Robust multidisciplinary analysis and optimization for conceptual design of flexible aircraft under dynamic aeroelastic constraints, Aerospace Science and Technology (2023) 108349.

[12] R. Grapin, Y. Diouane, J. Morlier, N. Bartoli, T. Lefebvre, P. Saves, J. H. Bussemaker, Regularized infill criteria for multi-objective Bayesian optimization with application to aircraft design, in: AIAA AVIATION 2022 Forum, 2022, p. 4053.

[13] A. Tran, M. Eldred, S. McCann, Y. Wang, srMO-BO-3GP: A sequential regularized multi-objective constrained Bayesian optimization for design applications, in: International Design Engineering Technical Conferences and Computers and Information in Engineering Conference, Vol. 83983, American Society of Mechanical Engineers, 2020, p. V009T09A015.

[14] R. Charayron, T. Lefebvre, N. Bartoli, J. Morlier, Multi-fidelity constrained Bayesian optimization, application to drone design, in: CAID 2021 Forum, 2021.

[15] R. Charayron, T. Lefebvre, N. Bartoli, J. Morlier, Pareto optimal fidelity level selection for multi-fidelity Bayesian optimization applied to drone design, in: 12 th EASN International conference, 2022.

[16] R. Charayron, T. Lefebvre, N. Bartoli, J. Morlier, Multi-fidelity Bayesian optimization strategy applied to overall drone design, in: AIAA SCITECH 2023 Forum, 2023, p. 2366.

[17] X. Ruan, P. Jiang, Q. Zhou, J. Hu, L. Shu, Variable-fidelity probability of improvement method for efficient global optimization of expensive black-box problems, Structural and Multidisciplinary Optimization 62 (6) (2020) 3021–3052.

[18] A. Tran, T. Wildey, S. McCann, sMF-BO-2CoGP: A sequential multi-fidelity constrained Bayesian optimization framework for design applications, Journal of Computing and Information Science in Engineering 20 (3) (2020).

[19] M. Meliani, N. Bartoli, T. Lefebvre, M.-A. Bouhlel, J. R. R. A. Martins, J. Morlier, Multi-fidelity efficient global optimization: Methodology and application to airfoil shape design, in: AIAA aviation 2019 forum, 2019, p. 3236.

[20] Q. Lin, A. Zheng, J. Hu, L. Shu, Q. Zhou, A multi-objective bayesian optimization approach based on variable-fidelity multi-output metamodeling, Structural and Multidisciplinary Optimization 66 (5) (2023) 100.

[21] D. Huang, A. Renganathan, M. A. Miller, Design of an aeroelastically scaled model in a compressible air wind tunnel facility using multifidelity multi-objective Bayesian optimization, in: AIAA SCITECH 2023 Forum, 2023, p. 2040.

[22] F. Irshad, S. Karsch, A. Döpp, Expected hypervolume improvement for simultaneous multi-objective and multi-fidelity optimization, arXiv preprint arXiv:2112.13901 (2021).

[23] T. Xue, L. Chen, J. Hu, Q. Zhou, A variable-fidelity multi-objective optimization method for aerospace structural design optimization, Engineering Optimization (2022) 1–16.

[24] A. Ariyarit, M. Kanazaki, Multi-fidelity multi-objective efficient global optimization applied to airfoil design problems, Applied Sciences 7 (12) (2017) 1318.

[25] F. Oukaili, Shape optimisation of overflow spillways., Ph.D. thesis, Université Paris Cité (2023).

[26] Y. He, J. Sun, P. Song, X. Wang, Variable-fidelity hypervolume-based expected improvement criteria for multi-objective efficient global optimization of expensive functions, Engineering with Computers 38 (4) (2022) 3663–3689.

[27] S. Belakaria, A. Deshwal, J. R. Doppa, Multi-fidelity multi-objective bayesian optimization: An output space entropy search approach, in:

Proceedings of the AAAI Conference on artificial intelligence, Vol. 34, 2020, pp. 10035–10043.

[28] C. E. Rasmussen, C. Williams, Gaussian processes for machine learning, vol. 1 (2006).

[29] D. G. Krige, A statistical approach to some basic mine valuation problems on the witwatersrand, Journal of the Southern African Institute of Mining and Metallurgy 52 (6) (1951) 119–139.

[30] G. Matheron, T. de Géostatistique Appliquée, I. Tome, Mémoires du bureau de recherche géologiques et minières, n. 14, Ed. Technip, Paris (1962).

[31] D. R. Jones, M. Schonlau, W. J. Welch, Efficient global optimization of expensive black-box functions, Journal of Global optimization 13 (4) (1998) 455–492.

[32] M. J. Sasena, Flexibility and efficiency enhancements for constrained global design optimization with Kriging approximations, Ph.D. thesis, Citeseer (2002).

[33] N. Bartoli, T. Lefebvre, S. Dubreuil, R. Olivanti, N. Bons, J. R. R. A. Martins, M.-A. Bouhlel, J. Morlier, An adaptive optimization strategy based on mixture of experts for wing aerodynamic design optimization, in: 18th AIAA/ISSMO Multidisciplinary Analysis and Optimization Conference, 2017, p. 4433.

[34] N. Bartoli, M.-A. Bouhlel, I. Kurek, R. Lafage, T. Lefebvre, J. Morlier, R. Priem, V. Stilz, R. Regis, Improvement of efficient global optimization with application to aircraft wing design, in: 17th AIAA/ISSMO Multidisciplinary analysis and optimization conference, 2016, p. 4001.

[35] J.-P. Chiles, P. Delfiner, Geostatistics: modeling spatial uncertainty, Vol. 497, John Wiley & Sons, 2009.

[36] H. Wackernagel, Multivariate geostatistics: an introduction with applications, Springer Science & Business Media, 2003.

[37] M. C. Kennedy, A. O'Hagan, Bayesian calibration of computer models, Journal of the Royal Statistical Society: Series B (Statistical Methodology) 63 (3) (2001) 425–464.

[38] L. Le Gratiet, Multi-fidelity Gaussian process regression for computer experiments, Ph.D. thesis, Université Paris-Diderot-Paris VII (2013).

[39] L. Le Gratiet, J. Garnier, Recursive co-Kriging model for design of computer experiments with multiple levels of fidelity, International Journal for Uncertainty Quantification 4 (5) (2014).

[40] F. Bachoc, Cross validation and maximum likelihood estimations of hyper-parameters of gaussian processes with model misspecification, Computational Statistics & Data Analysis 66 (2013) 55–69.

[41] D. Pavlyuk, Computing the maximum likelihood estimates: concentrated likelihood, EM-algorithm (2016).

[42] M. A. Bouhlel, J. T. Hwang, N. Bartoli, R. Lafage, J. Morlier, J. R. R. A. Martins, A python surrogate modeling framework with derivatives, Advances in Engineering Software (2019) 102662`doi:https://doi.org/10.1016/j.advengsoft.2019.03.005`.

[43] M. A. Bouhlel, N. Bartoli, A. Otsmane, J. Morlier, Improving Kriging surrogates of high-dimensional design models by Partial Least Squares dimension reduction, Structural and Multidisciplinary Optimization 53 (5) (2016) 935–952.

[44] K. S. Ng, A simple explanation of Partial Least Squares, The Australian National University, Canberra (2013).

[45] S. Wold, M. Sjöström, L. Eriksson, PLS-regression: a basic tool of chemometrics, Chemometrics and intelligent laboratory systems 58 (2) (2001) 109–130.

[46] A. G. Watson, R. J. Barnes, Infill sampling criteria to locate extremes, Mathematical Geology 27 (5) (1995) 589–608.

[47] N. Bartoli, T. Lefebvre, S. Dubreuil, R. Olivanti, R. Priem, N. Bons, J. R. R. A. Martins, J. Morlier, Adaptive modeling strategy for constrained global optimization with application to aerodynamic wing design, Aerospace Science and technology 90 (2019) 85–102.

[48] D. R. Jones, A taxonomy of global optimization methods based on response surfaces, Journal of global optimization 21 (2001) 345–383.

[49] A. A. Rahat, R. M. Everson, J. E. Fieldsend, Alternative infill strategies for expensive multi-objective optimisation, in: Proceedings of the genetic and evolutionary computation conference, 2017, pp. 873–880.

[50] E. Zitzler, L. Thiele, M. Laumanns, C. M. Fonseca, V. G. Da Fonseca, Performance assessment of multiobjective optimizers: An analysis and review, IEEE Transactions on evolutionary computation 7 (2) (2003) 117–132.

[51] M. T. Emmerich, K. C. Giannakoglou, B. Naujoks, Single-and multi-objective evolutionary optimization assisted by gaussian random field metamodels, IEEE Transactions on Evolutionary Computation 10 (4) (2006) 421–439.

[52] M. Zuluaga, G. Sergent, A. Krause, M. Püschel, Active learning for multi-objective optimization, in: International Conference on Machine Learning, PMLR, 2013, pp. 462–470.

[53] M. Zuluaga, A. Krause, M. Püschel, ε-PAL: an active learning approach to the multi-objective optimization problem, The Journal of Machine Learning Research 17 (1) (2016) 3619–3650.

[54] V. Picheny, Multiobjective optimization using gaussian process emulators via stepwise uncertainty reduction, Statistics and Computing 25 (6) (2015) 1265–1280.

[55] V. Picheny, A stepwise uncertainty reduction approach to constrained global optimization, in: Artificial intelligence and statistics, PMLR, 2014, pp. 787–795.

[56] K. Deb, A. Pratap, S. Agarwal, T. Meyarivan, A fast and elitist multiobjective genetic algorithm: NSGA-II, IEEE transactions on evolutionary computation 6 (2) (2002) 182–197.

[57] F. A. Viana, A tutorial on latin hypercube design of experiments, Quality and reliability engineering international 32 (5) (2016) 1975–1985.

[58] M. A. Bouhlel, J. T. Hwang, N. Bartoli, R. Lafage, J. Morlier, J. R. R. A. Martins, Surrogate modelling toolbox, `https://github.com/SMTorg/smt` (2022).

[59] R. Jin, W. Chen, A. Sudjianto, An efficient algorithm for constructing optimal design of computer experiments, in: International design engineering technical conferences and computers and information in engineering conference, Vol. 37009, 2003, pp. 545–554.

[60] R. Priem, N. Bartoli, Y. Diouane, T. Lefebvre, S. Dubreuil, M. Salaün, J. Morlier, SEGOMOE: Super efficient global optimization with mixture of experts, in: Workshop CIMI Optimization & Learning, 2018.

[61] H. Ishibuchi, H. Masuda, Y. Tanigaki, Y. Nojima, Modified distance calculation in generational distance and inverted generational distance, in: Evolutionary Multi-Criterion Optimization: 8th International Conference, EMO 2015, Guimarães, Portugal, March 29–April 1, 2015. Proceedings, Part II 8, Springer, 2015, pp. 110–125.

[62] T. Donateo, A. Ficarella, L. Spedicato, A. Arista, M. Ferraro, A new approach to calculating endurance in electric flight and comparing fuel cells and batteries, Applied energy 187 (2017) 807–819.

[63] L. W. Traub, Range and endurance estimates for battery-powered aircraft, Journal of Aircraft 48 (2) (2011) 703–707.

[64] M. N. Boukoberine, Z. Zhou, M. Benbouzid, Power supply architectures for drones-a review, in: IECON 2019-45th Annual Conference of the IEEE Industrial Electronics Society, Vol. 1, IEEE, 2019, pp. 5826–5831.

[65] B. J. Brelje, J. R. R. A. Martins, Electric, hybrid, and turboelectric fixed-wing aircraft: A review of concepts, models, and design approaches, Progress in Aerospace Sciences 104 (2019) 1–19.

[66] M. Hepperle, Electric flight-potential and limitations (2012).

[67] A. Gong, D. Verstraete, Role of battery in a hybrid electrical fuel cell UAV propulsion system, in: 52nd AIAA Aerospace Sciences Meeting, 2014.

[68] X. Zhang, L. Liu, Y. Dai, T. Lu, Experimental investigation on the online fuzzy energy management of hybrid fuel cell/battery power system for uavs, International journal of hydrogen energy 43 (21) (2018) 10094–10103.

[69] A. Gong, J. L. Palmer, G. Brian, J. R. Harvey, D. Verstraete, Hardware-in-the-loop simulation of a fuel-cell-based uav propulsion system using real-world flight data, in: Proceedings of the Fourth Australasian Unmanned Systems Conference, Australian Association for Unmanned Systems, 2014, p. 7.

[70] J. S. Gray, J. T. Hwang, J. R. R. A. Martins, K. T. Moore, B. A. Naylor, OpenMDAO: An open-source framework for multidisciplinary design, analysis, and optimization, Structural and Multidisciplinary Optimization 59 (4) (2019) 1075–1104.

[71] R. Falck, J. S. Gray, K. Ponnapalli, T. Wright, dymos: A Python package for optimal control of multidisciplinary systems, Journal of Open Source Software 6 (59) (2021) 2809. `doi:10.21105/joss.02809`.
URL `https://doi.org/10.21105/joss.02809`

[72] R. Lafage, S. Defoort, T. Lefebvre, WhatsOpt: a web application for multidisciplinary design analysis and optimization, in: AIAA Aviation 2019 Forum, 2019, p. 2990. `doi:10.2514/6.2019-2990`.
URL `https://doi.org/10.2514/6.2019-2990`

[73] J. P. Jasa, J. T. Hwang, J. R. R. A. Martins, Open-source coupled aerostructural optimization using python, Structural and Multidisciplinary Optimization 57 (4) (2018) 1815–1827.

[74] S. S. Chauhan, J. R. R. A. Martins, Low-fidelity aerostructural optimization of aircraft wings with a simplified wingbox model using openaerostruct, in: International Conference on Engineering Optimization, Springer, 2018, pp. 418–431.

[75] A. Chaudhuri, J. Jasa, J. R. R. A. Martins, K. E. Willcox, Multifidelity optimization under uncertainty for a tailless aircraft, in: 2018 AIAA Non-Deterministic Approaches Conference, 2018, p. 1658.

[76] R. Ibrahim, Market and cost analysis of hybrid-electric aircraft (2018).

[77] Mechanical properties of carbon fiber.
URL `http://www.performance-composites.com/carbonfibre/mechanicalproperties_2.asp`

[78] G. A. Wrenn, An indirect method for numerical optimization using the Kreisselmeier-Steinhauser function, Vol. 4220, National Aeronautics and Space Administration, Office of Management . . . , 1989.